ACS APPLIED MATERIALS & INTERFACES

www.acsami.org

Research Article

In Planta Nitrate Sensor Using a Photosensitive Epoxy Bioresin

Hussam Ibrahim, Shihao Yin, Satyanarayana Moru, Yunjiao Zhu, Michael J. Castellano, and Liang Dong*

Cite This: https://doi.org/10.1021/acsami.2c01988

Read Online

ACCESS | Metrics & More | Article Recommendations | Supporting Information

ABSTRACT: Nitrogen management through monitoring of crop nitrate status can improve agricultural productivity, profitability, and environmental performance. Current plant nitrate test methods require expensive instruments, time-intensive labor, and trained personnel. Frequent monitoring of *in planta* nitrate levels of the stalks in living plants can help to better understand the nitrogen cycle and the physiological responses to environmental variations. Although existing enzymatic electrochemical sensors provide high selectivity, they suffer from short shelf life, high cost, low-temperature storage requirement, and potential degradation over time. To overcome these issues, an artificial enzyme (vitamin B12 or VB12) and a two-dimensional material (graphene oxide or GO) are introduced into a conventional photoresist (SU8) to form a bioresin SU8-GO-VB12 that can be patterned with photolithography and laser-pyrolyzed into a carbon-based nanocomposite C-GO-VB12. The electrocatalytic activity of the cobalt factor in VB12, the surface enhancement properties of GO, and the porous feature of pyrolytic carbon are synergized through design to provide C-GO-VB12 with a superior ability to detect nitrate ions through redox reactions. In addition, laser writing-based selective pyrolysis allows applying thermal energy to target only SU8-GO-VB12 for selective pyrolysis of the bioresin into C-GO-VB12, thus reducing the total energy input and avoiding the thermal influence on the materials and structures in other areas of the substrate. The C-GO-VB12 nitrate sensor demonstrates a year-long shelf lifetime, high selectivity, and a wide dynamic range that enables a direct nitrate test for the extracted sap of maize stalk. For *in situ* monitoring of the nitrate level and dynamic changes in living maize plants, a microelectromechanical system-based needle sensor is formed with C-GO-VB12. The needle sensor allows direct insertion into the plant for *in situ* measurement of nitrate ions under different growth environments over time. The needle sensor represents a new method for monitoring *in planta* nitrate dynamics with no need for sample preparation, thus making a significant impact in plant sciences.

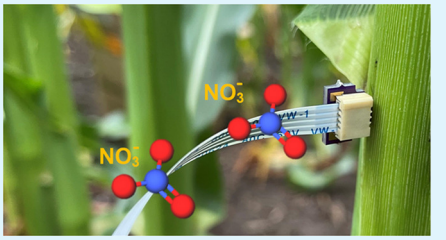

KEYWORDS: *nitrogen management, in planta sensors, nitrate sensors, wearable plant sensors, MEMS*

Downloaded via IOWA STATE UNIV on May 31, 2022 at 15:36:34 (UTC).
See https://pubs.acs.org/sharingguidelines for options on how to legitimately share published articles.

1. INTRODUCTION

The need for sustainable resource management in agriculture is increasingly urgent. As the most important macronutrient for crops, nitrogen is typically the greatest expense in crop fertilization, and nitrogen fertilizer management is crucial for the optimal productivity of crop production systems.[1] But, predicting an optimum nitrogen fertilizer input is extremely difficult because the optimum input varies by more than 50% from year-to-year and field-to-field owing to complex interactions among crop genetics, environment, and management.[2] Moreover, excessive nitrogen fertilizer inputs can severely impact the environment through nitrogen losses to surface and groundwater systems and emissions of the greenhouse gas nitrous oxide.[3,4]

The precise and timely monitoring of nitrogen availability in plants and soils has great potential to improve nitrogen fertilizer management by maintaining productivity and profitability while minimizing environmental nitrogen losses. Methods to measure nitrogen uptake and fixation in plants would also enhance our fundamental understanding of biophysical nitrogen dynamics, which is required to better manage the nitrogen cycle. Current tools for probing nitrogen status *in planta* primarily rely on destructive and time-intensive measurement methods, with low information content on the temporal characteristics of nitrogen uptake.[5] Alternative sensing methods that mainly rely on optical properties of plants suffer from chlorophyll saturation, genetic variation, atmospheric and soil interference, bulkiness, and high cost.[6,7] As a well-known method to inform nitrogen management, plant nitrate concentration measurements were performed on samples collected from the field and returned to the laboratory. These tests require relatively expensive instruments and laborious sample preparation (*e.g.*, cutting plants, ion extraction, and sample dilution) in addition to transport and storage.[8] Although ion chromatography and spectrophotometry used in the conventional plant nitrate tests provide high sensitivity and selectivity, they are not suitable for field application due to high cost, poor portability, and considerable consumption of agent and reagent. Low-cost portable sensors

Received: January 31, 2022
Accepted: May 16, 2022

© XXXX American Chemical Society

have recently been reported for monitoring nitrate availability in soils based on various sensing mechanisms, including ion-selective electrodes,[9,10] field-effect transistors,[11] microwave resonance,[12] reflectance spectrometers,[13] microfluidic electrophoresis chips,[14] and enzymatic electrochemical sensors.[15] However, tools are unavailable for direct measurement of the nitrate concentration *in planta* without complex sample preparations, which has limited our ability to evaluate the nitrogen needs of plants (deficient, marginal, optimal, or excessive) and benchmark the performance of nitrogen management.

Generally, enzyme-based electrochemical sensors provide high specificity to target molecules, where the sensing electrode is immobilized with a biological enzyme that can recognize a target molecule and catalyze the formation of the electroactive product for detection;[16] these sensors, however, are limited by degradation in the bioactivity of enzymes, a low-temperature requirement for storage, and a relatively high cost.[17] Therefore, there has been increasing interest in biomimetic artificial enzymes that exhibit similar behaviors to biological enzymes.[18] For example, owing to the presence of a cobalt (Co) factor surrounded by a ring structure of nitrogen and amino radicals, vitamin B12 (VB12) has an excellent electrocatalytic behavior of macrocycles; the ion-exchange properties of VB12 support the catalytic nitrogen and carbon group transfer and other reactions in living systems through the Co cations.[19] The redox chemistry of the Co cation renders VB12 feasible for electrochemical sensing. At the same time, carbon and carbon derivatives (*e.g.*, graphite, graphene, carbon nanotubes) have been widely used in electrochemical sensing electrodes due to their low cost, considerable conductivity, high chemical inertness, and a wide electrochemical potential window.[20] These carbon-based sensing electrodes can be manufactured using different means, such as inkjet printing, screen printing, and micromolding but often have a relatively low patterning resolution and are incompatible with the conventional low-cost semiconductor manufacturing process.[21] It is worth noting that some epoxy resin materials can be converted to carbon *via* thermal pyrolysis for applications, such as microelectromechanical systems,[22] biosensors,[23] energy storage devices,[24] stem cell scaffolds,[25] and dielectrophoresis.[26] Because thermal decomposition for carbon conversion takes place in a furnace or an oven with a vacuum or an inert atmosphere, high pyrolysis temperature (>600 °C[27]) may cause thermal damage to other materials and structures preformed on the substrate; such a temperature, for example, conflicts with complementary metal−oxide−semiconductor (CMOS) post-processing.[28] Direct laser-induced graphene (LIG)[29] has been realized on commercial polymer films (*e.g.*, polyimide, polybenzimidazole, polyether ether ketone, and polyetherimide) and even natural materials[30] through pyrolytic decomposition. The simplicity of laser synthesis has stimulated the research on developing a variety of LIG-based sensors, energy storage devices, and flexible electronics.[31−34] The LIG process, however, lacks flexibility in forming complex hierarchical LIG patterns with high spatial resolution and is restricted to using polymer-based substrates that are difficult to integrate with semiconductors toward monolithic integration of sensors and electronics.

This paper reports a plant nitrate sensor technology that can not only detect the nitrate concentration in the extracted sap of a cut stalk without the need for sample preparation but also monitor dynamic changes in nitrate concentration inside living plants. The electrochemical sensor utilizes a unique photosensitive epoxy bioresin composed of a conventional photoresist (SU8), an artificial enzyme (VB12), and two-dimensional graphene oxide (GO) nanosheets (Figure 1). Like an

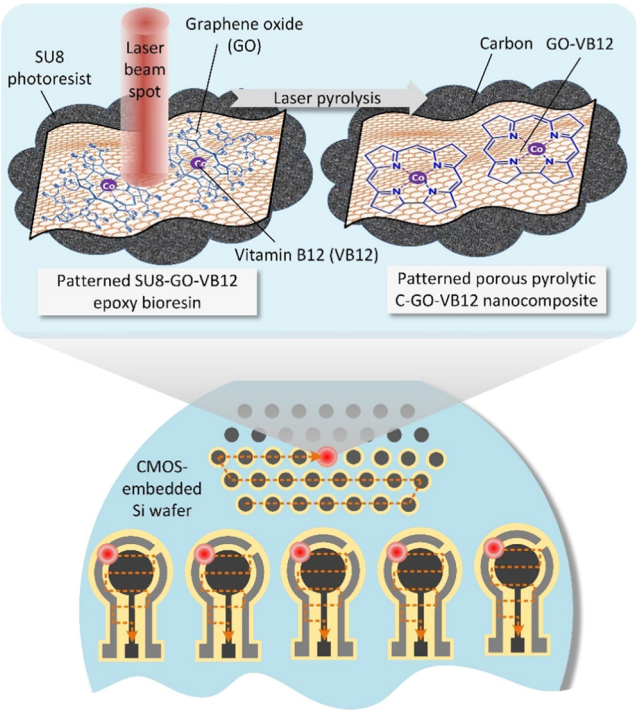

Figure 1. Photosensitive epoxy bioresin SU8-GO-VB12 consisting of the conventional photoresist (SU8), graphene oxide (GO), and vitamin B12 (VB12). The bioresin is spin-coated on a silicon wafer, patterned into high-resolution microstructures using photolithography, and pyrolyzed with a laser writing technique into a conductive nanocomposite of C-GO-VB12 that uses artificial enzyme VB12 as a biocatalyst for electrochemical sensing.

SU8 photoresist, the SU8-GO-VB12 bioresin retains the ability of high-resolution structural patterning *via* conventional photolithography and can be selectively pyrolyzed *via* laser writing to yield a pyrolytic carbon-based network of the artificial enzyme, namely C-GO-VB12, for electrochemical sensors. VB12 serves as a biocatalyst due to the presence of a Co factor, while the GO nanosheets can improve the efficiency of electron transfer to pyrolytic carbon during a redox reaction.[35] When a laser beam is programmed to apply thermal energy only to a target area of SU8-GO-VB12, thermal decomposition of the bioresin results in selective pyrolysis to form C-GO-VB12. The GO nanosheets are covalently bonded to the surface of pyrolytic carbon *via* rich carboxylic groups. VB12 is immobilized on the GO surface *via* the interaction between the amine group on VB12 and the oxygenic groups on GO. Through the selective pyrolysis of SU8-GO-VB12 into C-GO-VB12, the plant nitrate sensor is developed to detect nitrate ions in the extracted sap from cut stalks of maize plants. This electrochemical sensor recognizes nitrate ions by reducing NO_3^- to NO_2^- at a specific voltage potential, where the immobilized VB12 enhances the redox reaction through the Co^{2+}/Co^{3+} electrocatalytic activity of the cobalt factor in VB12 (Figure 2a,b). The sensor readout is comparable to conventional spectrophotometer measurements but unlike a spectrophotometer, it requires no dilution for sap due to the wide

https://doi.org/10.1021/acsami.2c01988
ACS Appl. Mater. Interfaces XXXX, XXX, XXX−XXX

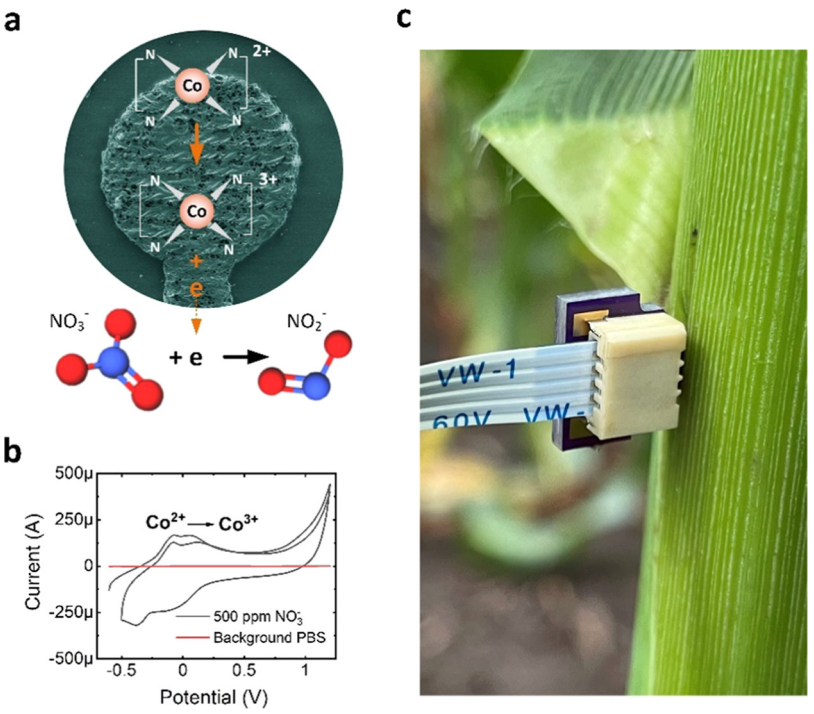

Figure 2. (a) Going from an oxidation state of Co^{2+} to Co^{3+} in VB12 loses an electron from the C-GO-VB12 electrode to reduce NO_3^- to NO_2^-. (b) Typical cyclic voltammogram of the C-GO-VB12 electrode exposed to 500 ppm concentration nitrate ions in a phosphate-buffered saline (PBS) solution, where the oxidation and reduction peaks occur due to the electrocatalytic activity of the cobalt factor in VB12. (c) MEMS-based plant sensor that integrates the C-GO-VB12-based sensing electrode shown in (a). The sensor is designed as a needle that can be inserted into the stalk of a maize plant to detect nitrate ions inside the stalk of a plant.

dynamic range of the sensor. The sensor also demonstrates high reusability and minimum performance degradation over time with a year-long storage lifetime that cannot be achieved with current biological enzyme-based electrochemical sensors.[36] More importantly, to eliminate laborious sample preparation required in a conventional stalk nutrient test, the C-GO-VB12 sensor is shaped into a needle through microelectromechanical system (MEMS) technology that enables the direct insertion of the sensor into the stalk for in situ monitoring of dynamic changes in the nitrate level in living plants (Figure 2c).

2. RESULTS AND DISCUSSION

2.1. Structural and Thermal Analysis. Conventional photolithography was used to produce SU8-GO-VB12 patterns with about 10 μm patterning resolution in the planar directions and up to 5 high aspect ratio; the sequential laser pyrolysis resulted in the corresponding C-GO-VB12 patterns (Figure 3a). The overall shape of the C-GO-VB12 structures remained but their spatial resolution was reduced due to the laser-induced decomposition for carbon conversion (Figure 3b). Nevertheless, the present method is advantageous over the LIG process in terms of patterning resolution and control over the thickness and the structure of pyrolytic products. For example, hierarchical structures of C-GO-VB12 with multiple layers (the bottom of Figure 3b) were also realized.

To examine the thermal and morphological stability of SU8-GO-VB12 during the pyrolysis process, thermal gravimetric analysis (TGA; temperature range: from 20 to 900 °C; ramp rate: 5 °C/min) was conducted on SU8-GO-VB12 in a conventional furnace (Figure 4a). The analysis helped to determine the minimum temperature required for laser pyrolysis. There occurred a total of 3.5% weight loss accompanying a color change to black at the end of TGA, among which an initial 0.4% weight loss was observed around 300 °C (attributed to the loss of solvents), a 1.1% weight loss from 300 and 440 °C (may be due to the release of axially coordinated molecules with the Co center and the removal of nitro and phenyl groups), and another 0.6% weight loss from 440 to 600 °C (perhaps associated with the decomposition of a cobalt phthalocyanine-like polymer). As the temperature increased above 600 °C, the weight loss became distinct accompanying a 24% reduction in the height of the patterns. Therefore, a minimum temperature of 600 °C was required for the laser pyrolysis of SU8-GO-VB12, which agreed with the reported temperature for converting the pure SU8 into pyrolytic carbon. Next, to assure a greater than 600 °C temperature of the SU8-GO-VB12 material during laser pyrolysis, a thermal imaging method (FLIR E6-XT Teledyne FLIR; Wilsonville, OR) was employed to visualize the temperature profile at the laser spot (Figure S1a). The laser beam (beam diameter: 200 μm; input power: 3.32 W; exposure time: 5 s) was programmed to write across the SU8-GO-VB12 pattern. The hottest white spot in the image corresponded to the laser spot, where the displayed 550 °C was limited to the maximum measurable temperature of the used imager. Therefore, thermal simulation was conducted using finite element analysis-based software (COMSOL). The result showed that the temperature at the beam spot could reach 820 °C, which was sufficient for pyrolysis (Figure S1b). The temperature gradient from the laser spot to the surroundings implies a reduced thermal influence on the materials and structures in other areas of the silicon substrate.

https://doi.org/10.1021/acsami.2c01988
ACS Appl. Mater. Interfaces XXXX, XXX, XXX−XXX

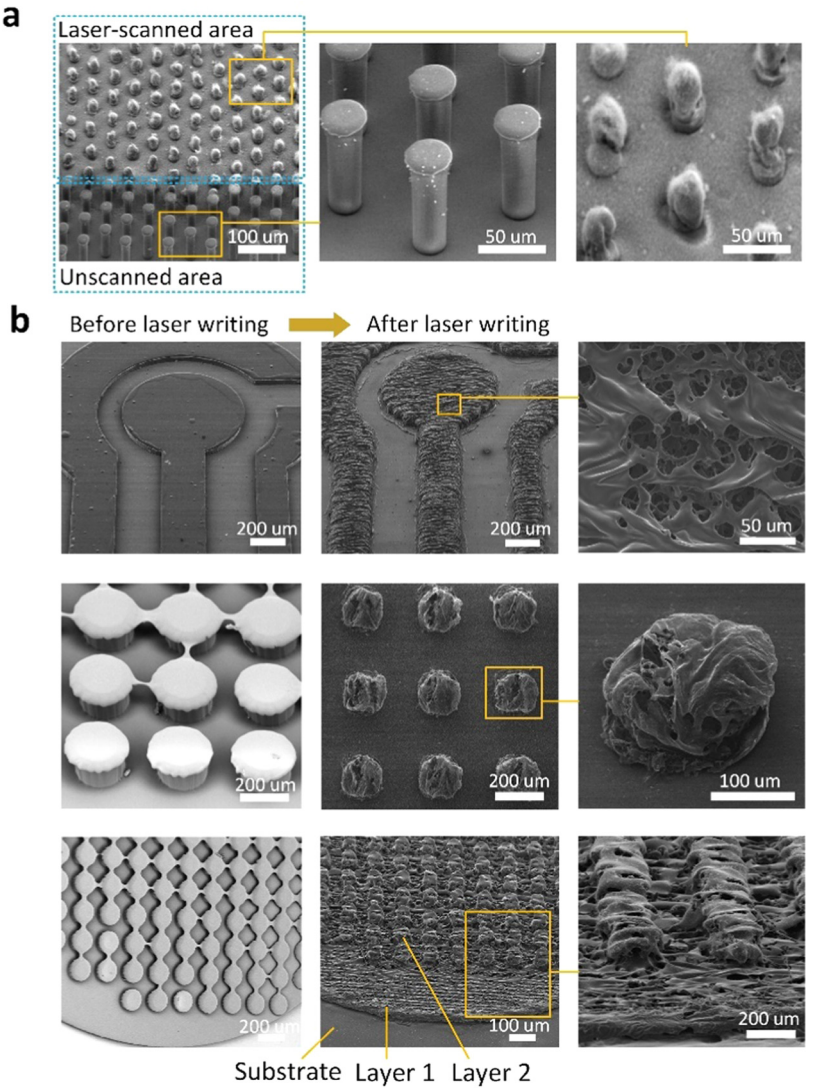

Figure 3. Scanning electron microscopy (SEM) images for various microstructures of the bioresin before and after selective pyrolysis with a laser. (a) Single-layer microstructures and (b) two-layer hierarchical microstructures.

To verify the presence of Co in the laser-pyrolyzed samples, X-ray photoelectron spectroscopy (XPS) was used to analyze the surface chemical states of the elements in C-GO-VB12, as well as in C-GO for comparison (Figure 4b). The C-GO sample exhibits the characteristic peaks for C (285.0 eV) and O (531.5 eV), while the C-GO-VB12 sample has two additional peaks for N (399.5 eV) and Co (781.2 and 796.4 eV). Both the characteristic peaks for Co are assigned to the Co−N*x* coordination. The accompanying two intense satellite peaks at 789.1 and 804.9 eV demonstrate that Co^{2+} in C-GO-VB12 is in the high-spin state.[37,38] The intensity of the Co 2p 3/2 peak at 781.2 eV is higher than those of Co oxide at 788.0 eV and metallic Co at 804.0 eV, thus confirming that Co^{2+} exists primarily in the form of Co−N*x*. The seeding of Co species within the VB12 framework is tetra-coordinated with the N atoms; thus, the Co−N*x* coordination in GO-VB12 may be defined as Co−N4 coordination. By deconvoluting the high-resolution C 1s spectrum of C-GO-VB12 (Figure S2a), three different peaks appear at the binding energies of 284.5, 285.9, and 288.1 eV that correspond to graphitic C (C−C/C═C) units, C−O, and sp^2 C atoms bonded to N (N−C═N), respectively, within the CN matrix. Also, the O 1s spectrum of C-GO-VB12 (Figure S2b) exhibits two peaks at 531.5 and 532.8 eV that correspond to O−H/O−C and O═C moieties, respectively. No oxygen components related to metal oxides (M−O) are observed in the O 1s spectrum of C-GO-VB12, indicating that the observed oxygen components mainly originate from the oxygenic functional groups of GO rather than from metal oxides. The N 1s spectra (Figure S2c) reveal that three contributions at 398.6, 399.9, and 401.4 eV for C-GO-VB12 are attributed to Co−N4, pyrrolic N, and graphitic N, respectively. Despite that the binding energy at 398.6 eV can also represent the C−N/C═N components, the presence of Co−N4 coordination in C-GO-VB12 is confirmed by the Co 2p peak (Figure S2d). Further, Raman spectroscopy shows that C-GO-VB12 exhibits D and G band peaks at 1341 cm^{-1} (associated with nanocrystalline carbon) and 1605 cm^{-1} (sp^2-bonded amorphous carbon material), respectively (Figure S3). Essentially, the origin of the G band in C-GO-VB12 is owing to the defect-induced double-resonant scattering, while the D band peak is caused by the intervalley scattering process. Energy-dispersive X-ray spectroscopy (EDS) shows that the C-GO sample (Figure S4a) has abundant C and O (Figure 4c), while the C-GO-VB12 sample (Figure S4b) has not only C

https://doi.org/10.1021/acsami.2c01988
ACS Appl. Mater. Interfaces XXXX, XXX, XXX−XXX

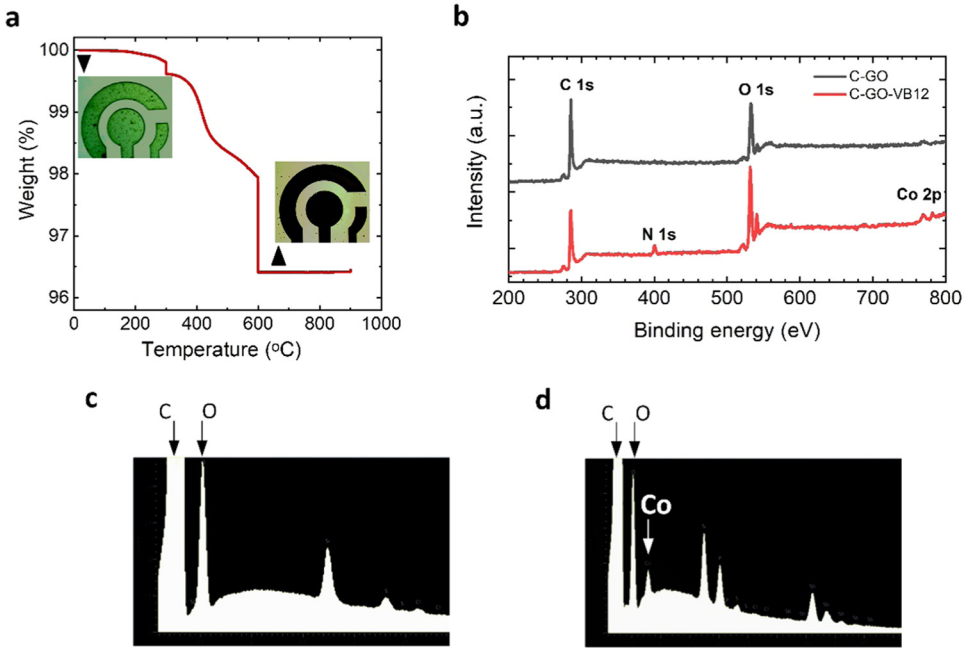

Figure 4. TGA analysis during converting SU8-GO-VB12 to C-GO-VB12, and X-ray photoelectron spectroscopy (XPS) and energy-dispersive X-ray spectroscopy (EDS) examination of Co in C-GO-VB12. (a) TGA for SU8-GO-VB12. The insets show the as-patterned SU8-GO-VB12 and the pyrolyzed C-GO-VB12. (b) XPS spectra for the pyrolytic C-GO-VB12 and C-GO (control). (c, d) EDS spectra for the pyrolytic C-GO (a) and C-GO-VB12 (b). The Co peak appears in C-GO-VB12 due to the presence of VB12.

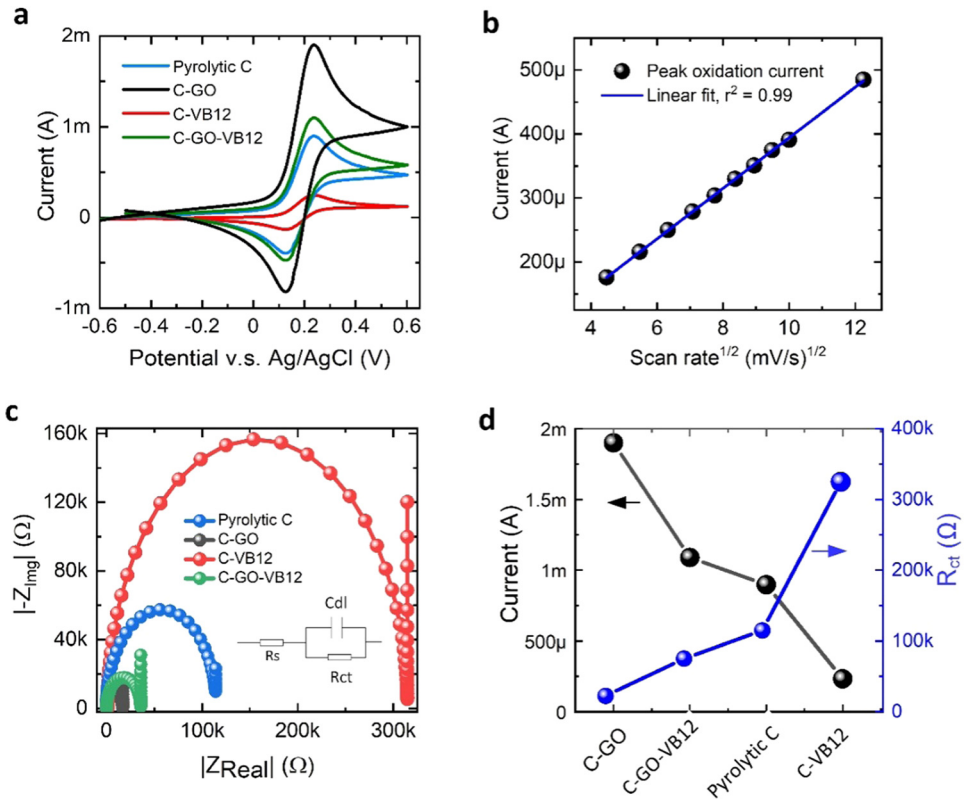

Figure 5. Electrochemical characterization of the C-GO-VB12 electrode. (a) Cyclic voltammetry (CV) showing the redox behaviors of the pyrolytic C, C-GO, C-VB12, and C-GO-VB12 electrodes. The CV measurements (scan rate: 150 mV/s) were conducted with 10 mM $K_3[Fe(CN)_6]$ + 100 mM KCl as a redox electrolyte. (b) Peak oxidation current I_{ox} *versus* the square root of the scan rate from 30 to 150 mV/s. (c) Nyquist plots from the pyrolytic C, C-GO, C-VB12, and C-GO-VB12 electrodes obtained using the same redox electrolyte as that used in (a). The inset shows the Randles circuit where R_{ct} is the charge transfer resistance, C_{dl} is the capacitance of the dielectric layer, and R_s is the solution resistor. (d) Charge transfer resistance (R_{ct}; right axis) and the peak oxidation current (I_{ox}, left axis) for the pyrolytic C, C-GO, C-VB12, and C-GO-VB12 electrodes.

https://doi.org/10.1021/acsami.2c01988
ACS Appl. Mater. Interfaces XXXX, XXX, XXX−XXX

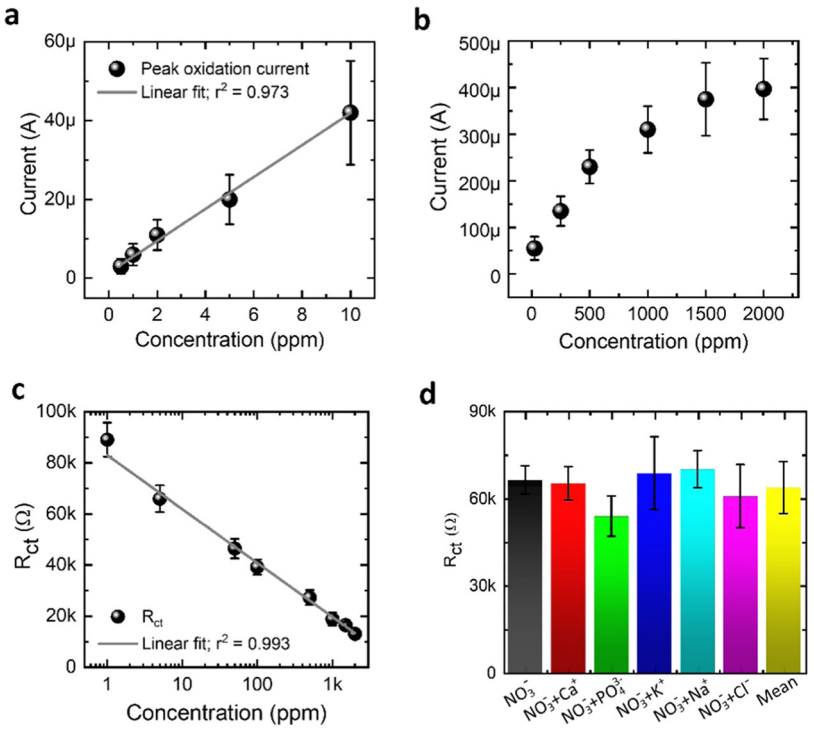

Figure 6. Characterization of the C-GO-VB12 nitrate sensor. (a, b) Calibration curves for the peak oxidation current *versus* nitrate ion concentration obtained based on the CV responses of the C-GO-VB12 sensor to nitrate concentrations from 0.2 to 10 ppm (a) and from 20 to 2000 ppm (b). (c) Calibration curve for the charge transfer resistance R_{ct} *versus* nitrate ion concentration in a range from 0.2 to 2000 ppm obtained using the electrochemical impedance spectroscopy technique. The sensor calibrations in (a−c) were performed using standard nitrate solutions. (d) R_{ct} of the sensor in the presence of different interference ions, including Ca^{2+}, PO_4^{3-}, K^+, Na^+, and Cl^-. The sensor here was exposed to 5 ppm concentration nitrate ions alone and a mixture of 5 ppm concentration nitrate ions and one of the interference ions mentioned above at a 500 pm concentration of each type.

and O but also Co, thus further affirming that Co is still present for catalytic activity after the laser pyrolysis process (Figure 4d).

2.2. Electrochemical Characterization of C-GO-VB12. Cyclic voltammetry (CV) determined an optimum amount of VB12 in SU8-GO-VB12 for generating a high peak oxidation current (I_{ox}) from the converted C-GO-VB12 electrode. With increasing VB12 concentration from 17 to 83 mg/mL under a fixed GO concentration at 6.6 mg/mL, the SU8-GO-VB12 solution became darker; all of the converted corresponding C-GO-VB12 samples exhibited the oxidation and reduction peaks occurring between −0.6 and 0.6 V, arising from the Co^{2+}/Co^{3+} redox reaction in VB12 (Figure S5). The C-GO-VB12 sample with an 83 mg/mL VB12 concentration produced the highest current I_{ox} = 250 μA at a scan rate of 50 mV/s. Introducing higher concentrations of VB12 to the SU8-GO-VB12 solution led to sediments at the bottom of the solution.

The optimized C-GO-VB12 electrode (83 mg/mL VB12 concentration in SU8-GO-VB12) and three counterparts (pyrolytic C, C-GO, and C-VB12 electrodes) were examined with the CV technique at a scan rate of 150 mV/s to explore the maximum redox activity. Figure 5a shows that the pyrolytic C electrode produced I_{ox} = 0.8 mA. The introduction of a 6.6 mg/ml concentration GO into SU8 led to an increase of I_{ox} to 1.89 mA from the C-GO electrode due to the conducting nature of GO. With the optimum amount of VB12 added to SU8, the C-VB12 electrode produced a lower I_{ox} at 0.25 mA, possibly because of the nonconducting nature of VB12. Compared with the C-VB12 electrode, the C-GO-VB12 electrode had a greater I_{ox} at 1.1 mA because the −COOH group presented in GO may enable sufficient bonding with VB12 through $-NH_2$ groups. Also, the I_{ox} value from the C-GO-VB12 electrode was directly proportional to the square root of the scan rate (Figures 5b and S6), indicating that the C-GO-VB12 electrode exhibited a surface-controlled process. Further, all of the C-GO-VB12 and counterpart electrodes were examined with electrochemical impedance spectroscopy (EIS), showing that the electrodes with lower charge transfer resistance values (R_{ct}; obtained from the Nyquist plots in Figure 5c) presented greater I_{ox} values (obtained from the CV curves in Figure 5a).

2.3. Nitrate Sensor Characterization. The redox reaction of Co^{2+}/Co^{3+} in VB12 supported nitrate detection with the C-GO-VB12 electrode. Figure 2b shows a typical redox activity of Co^{3+} ions in the presence of nitrate ions in a phosphate-buffered saline (PBS) solution. The C-GO-VB12 sensor exhibited almost no response (I_{ox} < 10 μA) to the background PBS solution. When exposed to a 500 ppm nitrate concentration, the sensor generated a peak oxidation current I_{ox} of 124 μA at −0.05 V due to the Co^{2+}/Co^{3+} redox reaction. Figure 6a shows the CV calibration plot of the sensor to low nitrate concentrations from 0.2 to 10 ppm. With increasing nitrate concentration, the oxidation peak current I_{ox} increased due to generating more electrons through the redox reaction at −0.05 V (Figure S7a). A linear fit for the calibration plot indicates a sensitivity of 4.046 μA/ppm with an *r*-square value of 0.98 (Figure 6a). The current increased at a slower rate toward saturation for higher nitrate concentrations from 20 ppm to 2000 ppm (Figures 6b and S7b). Next, the EIS technique was used to calibrate the C-GO-VB12 sensor. The

https://doi.org/10.1021/acsami.2c01988
ACS Appl. Mater. Interfaces XXXX, XXX, XXX−XXX

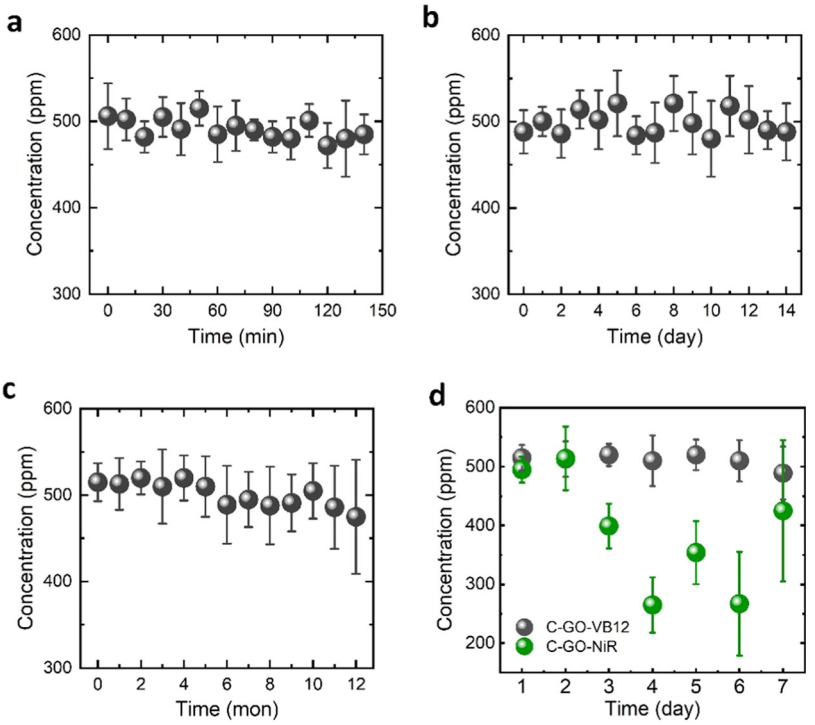

Figure 7. (a–c) Stability and repeatability of the C-GO-VB12 sensor over different time scales: 140 min (a), 12 days (b), and 12 months (c). (d) Stability comparison between the C-GO-VB12 sensor and the C-GO-NiR sensor when both were exposed to 500 ppm concentration nitrate ions in the standard solution once a day for 7 days.

R_{ct} value of the sensor decreased with increasing nitrate concentration (Figure 6c) because nitrate ions were reduced to nitrite producing electrons. The sensitivity of R_{ct} to the nitrate concentration was −28.95 kΩ/ppm with $r^2 = 0.99$. The limit of detection (LOD) for nitrate ions was calculated to be about 0.2 ppm by the $3\sigma_b/m$ criteria,[39] where σ_b and m present the standard deviation for I_{ox} and the slope of the calibration curve, respectively. The EIS technique was conjugated with the sensor for stalk nitrate measurements described later.

The C-GO-VB12 sensor demonstrated the ability to distinguish the target nitrate ion from interference ions, such as Ca^{2+}, Na^+, K^+, Cl^-, and PO_4^{3-} (Figure 6d). Here, the sensor was exposed to a 5 ppm concentration nitrate solution and then a mixture of the nitrate ion (5 ppm) and each of the concerned interference ions (500 ppm each). With 2 orders of magnitude higher concentration than nitrate ions under test, these interference ions had only a limited influence on the R_{ct} value of the sensor with the overall relative standard deviation (RSD) of 12.3%. The selectivity of the sensor toward nitrate ions was achieved by reducing NO_3^- to NO_2^- at a specific voltage potential of −0.05 V determined by the cyclic voltammetric responses (Figure S7). Here, the EIS measurement (Figure 6d) was conducted at the same voltage potential for detecting nitrate ions; the result indicates that the redox reaction of the sensor with nitrate ions dominated the reactions with the interference ions under test.

Figure 7a–c shows the stability and repeatability of the sensor for detecting a 500 ppm concentration standard nitrate solutions over different time scales (hours, days, and months). Between two consecutive measurements, the sensor was cleaned with a PBS solution, dried with compressed air, and stored in a Petri dish at room temperature. Over the time scales from short to long time periods, the measured nitrate concentrations had a mean value of 492, 496, and 511 ppm with an RSD of 11.5, 11.8, and 10.3%, respectively, demonstrating considerable long-term stability and repeatability for the detection of nitrate ions. Further, the C-GO-VB12 sensor was compared with a biological enzyme-based nitrate sensor in terms of stability and reusability (Figure 7d). This counterpart device was designed to be identical to the C-GO-VB12 sensor, except for using the C-GO material as a working electrode, whose surface was functionalized with nitrate reductase or NiR (NAD[P]H (*Aspergillus niger*; Sigma Aldrich, St. Louis, MO)), a biological enzyme specific to nitrate ions.[40] The NiR enzyme molecules were bonded to the surface of the C-GO electrode *via* EDC-NHS to form the C-GO-NiR sensor for comparison. For repeatedly detecting 500 ppm concentration nitrate ions in the standard solution once a day for 7 days, the counterpart sensor was found to significantly degrade after the first two measurements (Figure 7d). The stability and reusability of the NiR enzyme may be impacted by enzyme inactivation and enzyme loss. In contrast, the C-GO-VB12 sensor with the Co–N4 macrocycle exhibited little degradation, as evident by the relatively stable output of the nitrate concentration.

2.4. Nitrate Measurement of the Extracted Plant Sap.

The C-GO-VB12 sensor demonstrated the ability to measure nitrate concentrations in sap extracted from the cut stalk of maize plants (the number of plants $n = 3$; genotype: B73; measured at the 10 leaf growth stage; Figure 8a,b). Each plant provided three 2 cm long stalk cuttings in the second (low stalk), fourth (middle), and fifth (high) leaf internodes. Because a conventional spectrophotometer provided a narrow dynamic range (up to ∼20 ppm), the extracted sap samples from the low, middle, and high cut stalks were diluted in PBS for the spectrophotometry analysis with dilution factors of $m =$ 10, 100, and 1000, respectively (Figure 8a). In contrast, the sensor had a wide dynamic range (up to ∼2000 ppm) that

https://doi.org/10.1021/acsami.2c01988
ACS Appl. Mater. Interfaces XXXX, XXX, XXX–XXX

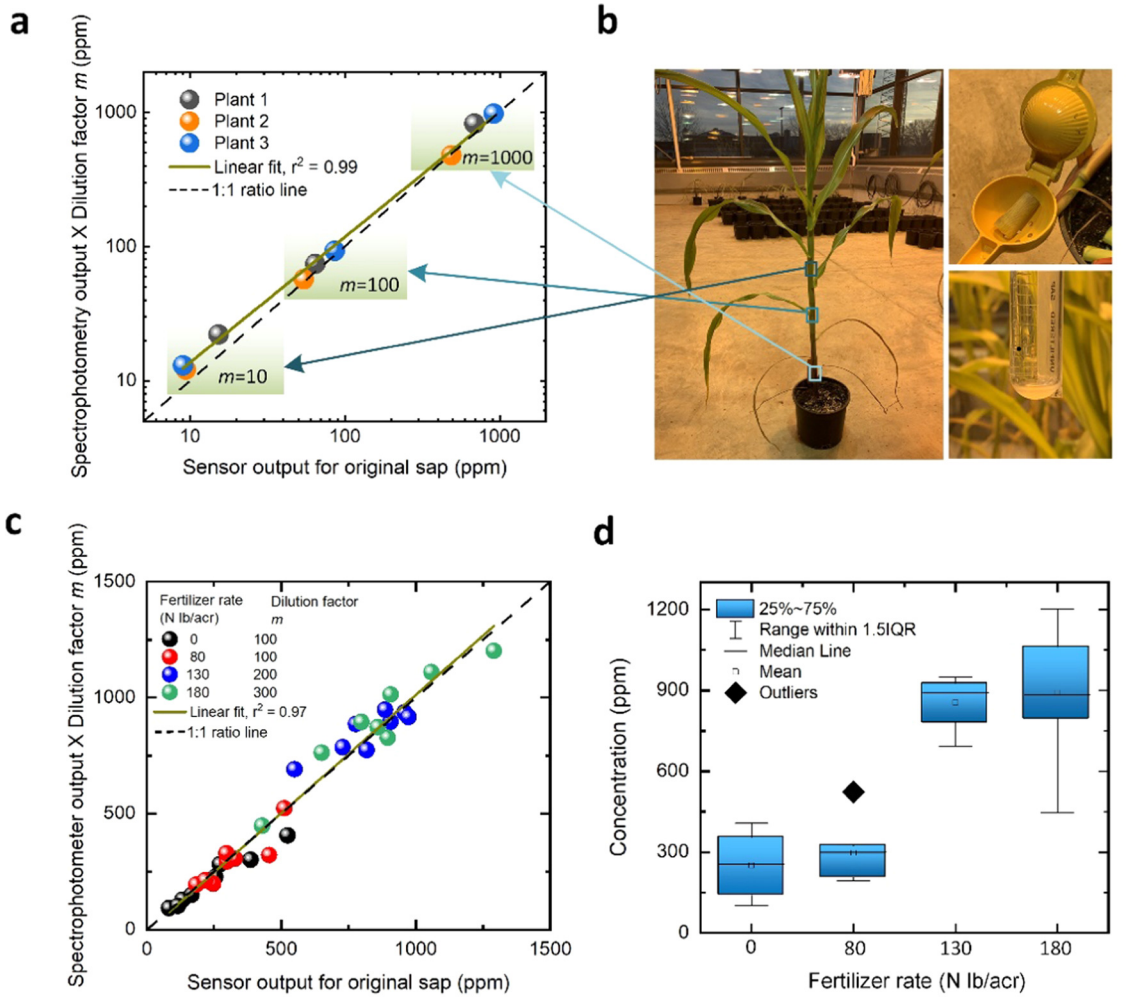

Figure 8. Detection of nitrate ion concentration in the extracted stalk of maize plants grown in the greenhouse and the field. (a) Comparison between the sensor output and the spectrophotometer measurement for the nitrate concentration in the extracted sap of the cut stalks at the second (low), fourth (middle), and fifth (high) internodes above the ground. (b) Optical image showing the internodes cut from the stalk and used to extract the sap with a juice squeezer. (c) Comparison between the sensor output and the spectrophotometer measurement for the nitrate concentration in the extracted sap from the cut stalks of field-grown maize plants that received four nitrogen fertilizer treatments, including 0, 80, 130, and 180 N lb/acr. For both (a) and (c), the sensor was exposed to 30 μL of the original sap per test, while the spectrophotometer was used to test the diluted sap samples by different dilution factors *m*. The spectrophotometer readings were multiplied by the value of m for comparing with the sensor output. (d) Sensor-measured nitrate concentrations of the original sap extracted from the maize plants with the four nitrogen fertilizer treatments mentioned in (c).

covered the nitrate concentrations of the original sap, which spanned 2 orders of magnitude. The original sap was tested with the sensor using the EIS technique. Figure S8a shows the Nyquist plots from the sensor when exposed to the original sap from the high, middle, and low-cut stalks. Lower stalks had a higher nitrate level than the upper stalks (Figure 8a), which is a well-documented pattern. The spectrophotometer readout for the diluted sap was multiplied by the dilution factor *m* for comparing with the sensor readout. There appeared only minor discrepancies in the nitrate concentrations obtained using these two methods. All of the data points were close to the unity slope, indicating high measurement accuracy of the sensor.

Further, the C-GO-VB12 sensor was used to measure nitrate concentrations in the extracted sap from the cut stalks in the second internode of field-grown maize plants (genotype: B73; growth stage: V7) that received four N fertilizer treatments (0, 80, 130, and 180 N lb/acr; the number of plants: $n = 8$ for each treatment). In conjunction with the EIS measurement (Figure S8b), the sensor reveals considerable plant-to-plant variations in stalk nitrate even in the same internode under the same fertilizer rate (Figure 8c). A high correlation ($r^2 = 0.97$) and nearly unity slope were achieved between the sensor and spectrophotometer outputs. Overall, the stalk nitrate level exhibited an increasing trend with increasing N fertilizer rate (Figure 8d). The plausible reason for no obvious difference between 0 and 80 lb/acr of N fertilizer treatment is the following: as plants uptake nitrate, they reduce the nitrate to amino acids for protein production, which can occur in roots, shoots, and leaves. As plants become increasingly free of nitrogen limitation, more nitrate may be transported to leaves prior to reduction because there is more energy available for nitrate reduction in the leaves. This pattern has been previously demonstrated in the xylem sap of maize.[41] Hence, the low response of stalk nitrate to 80 lb/acr of N fertilizer treatment indicates that nitrate may be completely reduced prior to transport through the stalk xylem, resulting in no apparent difference in stalk nitrate. In contrast, the stalk nitrate

https://doi.org/10.1021/acsami.2c01988
ACS Appl. Mater. Interfaces XXXX, XXX, XXX−XXX

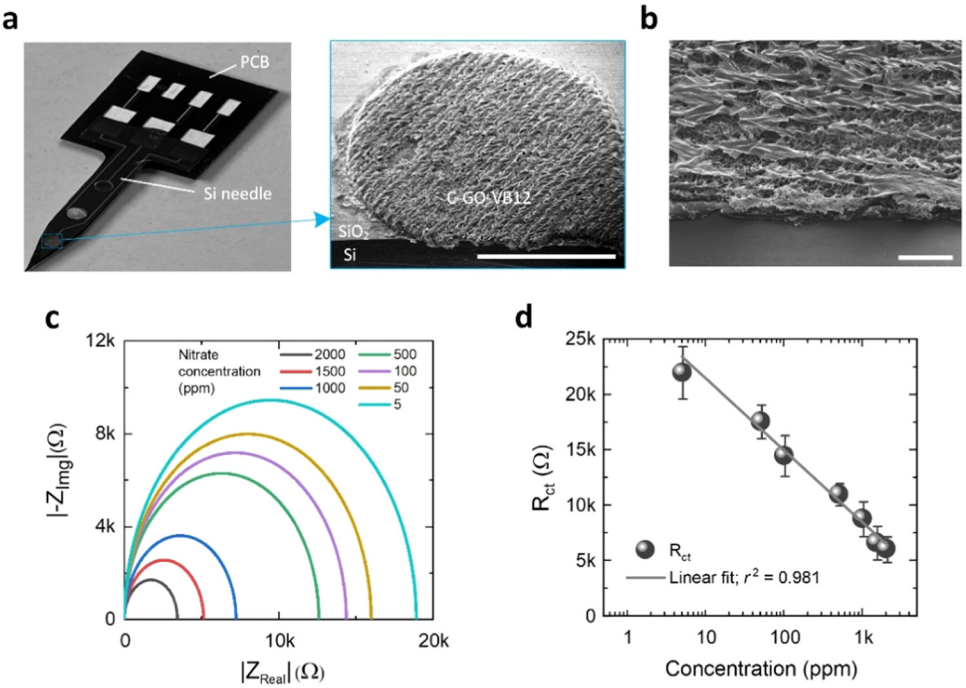

Figure 9. MEMS-based C-GO-VB12 needle sensor for *in situ* monitoring of the stalk nitrate concentration. (a) Photo of the needle sensor amounted to a PCB with electrical contact pads. The inset shows the SEM image for the tip of the sensor containing the C-GO-VB12 electrode. Scale bar: 500 μm. (b) SEM image for a close-up of the C-GO-VB12 electrode at the tip of the needle sensor. Scale bar: 100 μm. (c) Nyquist spectra obtained from the needle sensor exposed to different nitrate concentrations. (d) Calibration curve for charge transfer resistance R_{ct} of the C-GO-VB12 electrode as a function of nitrate concentration.

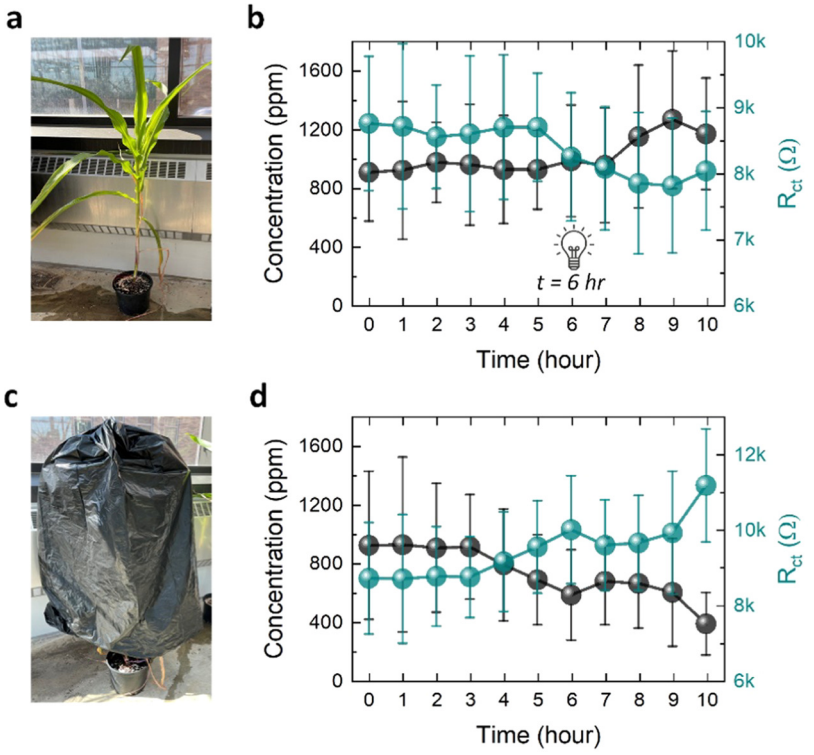

Figure 10. *In situ* monitoring of the stalk nitrate concentration over time using the needle sensor. (a) Photo of an uncovered maize plant. (b) Measured stalk nitrate concentrations of the uncovered maize plant for 10 h (left) and corresponding R_{ct} values obtained from the inserted needle sensor. (c) Photo of a light-shielded maize plant with a black plastic bag. (d) Measured stalk nitrate concentrations of the light-shielded maize plant and corresponding R_{ct} values. The uncovered plant in (a) exhibited an increase in the stalk nitrate level when the light intensity increased at time t = 6 h, while the light-shielded plant in (c) exhibited a reduction in the nitrate level under the same condition.

https://doi.org/10.1021/acsami.2c01988
ACS Appl. Mater. Interfaces XXXX, XXX, XXX−XXX

concentration increased significantly for the N fertilizer application rate of 130 lb/acr, indicating less N limitation (*i.e.*, an increased rate of N uptake by roots from the soil) with a greater proportion of nitrate reduction occurring in the leaves. High portability, rapidity, and accuracy make the C-GO-VB12 sensor technology extremely promising for *in situ* plant nitrate measurement.

2.5. MEMS Needle Sensor-Based *In Situ* Stalk Nitrate Measurement. A needle-shaped C-GO-VB12 sensor was fabricated using MEMS technology for *in situ* monitoring of stalk nitrate in maize plants without the need of extracting the sap from the cut stalk, thus further simplifying the stalk nitrate measurement. The layout and shape of the WE, CE, and RE were adjusted to fit the form of the needle sensor. The fabrication process for the sensor is described in Section 4 and Figure S9. The fabricated needle sensor was attached and wire-bonded to a small printed circuit board that had three electrical contact pads (Figure 9a,b). A lightweight cable (UXCELL Flexible Flat Cable; 4 Pins; 0.5 mm Pitch) was gently attached to the stalk, connecting the PCB to a datalogger placed on the ground. The sensor was calibrated with the EIS technique using standard nitrate ion solutions (Figure 9c,d).

To conduct *in situ* monitoring of changes in the stalk nitrate level of plants, the needle sensor was inserted into the stalks of maize plants (genotype: B73; growth stage: V10) grown in the pots in the greenhouse (fertilizer: ironite mineral supplement containing 1% urea nitrogen and slow-release fertilizer from Harrell's LLC; model #: 17-5-12). The needle part of the sensor was then left in the second leaf internode of the stalk for 10 h for direct measurement of the nitrate concentration at a frequency of once per hour. The insertion depth of the needle was ∼10 mm into the stalk. This pilot experiment involved exposing one group of maize plants (number of plants: $n = 6$) to normal growth light conditions (Figure 10a) and shielding light in the other group ($n = 6$) with black bags (Figure 10c). The obtained Nyquist spectra are shown in Figure S10. The stalk nitrate level of the plants in the dark environment was found to gradually decrease to a level around 600 ppm at time $t = 6$ h (Figure 10d); however, the unshielded plants reduced their stalk nitrate at a slower rate in the same time frame (Figure 10b). Subsequently, the light intensity in the greenhouse increased. Consequently, the unshielded plants responded by increasing the stalk nitrate concentration to a higher level around 1000 ppm, while the nitrate concentration in the shielded plants continued to drop. The observed difference in the stalk nitrate between these two groups of plants is almost certainly associated with photosynthesis: compared to the plants under the light that can transpire, photosynthesize, and uptake nitrate from the soil solution, the plants in the dark close stomata, stopping transpiration, photosynthesis, and uptake nitrate ions from the soil solution. At the same time, respiration should have allowed the plants to continue nitrate reduction to amino acids.

Compared to other electrochemical sensors for the detection of nitrate ions (Table S1), our sensor offered a wide dynamic range of nitrate concentrations from 0.2 to 2000 ppm, while the biological enzyme (NiR)-based nitrate sensor had a much narrower range only up to about 450 ppm, possibly due to the saturation of binding sites at the NiR enzyme.[15,40] It should be noted that conventional spectrophotometers provide high accuracy in determining the nitrate ion concentration with a 0.1 ppm resolution but enable only a narrow dynamic range of detection up to 20 ppm nitrate concentration. Because the actionable range of corn stalk nitrate test generally spans a 700−2000 ppm nitrate concentration, this requires complex procedures to dilute and prepare samples prior to conventional spectrophotometry analysis, adding cost and analytical error while precluding in-field or *in planta* analysis. In contrast, the C-GO-VB12 sensor could enable direct measurement without sample processing due to the wide dynamic range. Also, the high sensitivity of the sensor may be due to the enhanced catalytic reactivity of C-GO-VB12 that contains porous pyrolytic carbon and GO nanosheets with considerable conductivity and surface area. The C-GO-VB12 sensor outperforms other electrochemical nitrate sensors in terms of reusability and stability as evident by a year-long shelf time at room temperature.

Current plant nitrate test methods require expensive instruments, tedious and time-intensive labor, and trained personnel, and therefore are not suitable for field measurements. The direct *in planta* measurement of the stalk nitrate concentration together with the wide dynamic range of the sensor eliminated the need for time-consuming sample preparation including tedious sample dilutions that are necessary with conventional methods. Further, the needle sensor allowed monitoring of dynamic changes in the stalk nitrate concentration with a relatively high temporal resolution. *In planta* nitrogen status and dynamics are key physiological parameters at the interface between plant responses and primary determinants of phenotype such as genotype and environmental conditions. Therefore, the presented needle sensor technology will solve the problem facing the existing plant nitrogen measurement approaches as a new method for monitoring *in planta* nitrate uptake, thus making a more significant impact in plant sciences.

3. CONCLUSIONS

We have introduced GO and VB12 into a conventional SU8 photoresist to form a photosensitive epoxy bioresin that could be photopatterned and laser-pyrolyzed to realize artificial enzyme-based electrochemical nitrate sensors. The C-GO-VB12 material served as a catalyst network for identifying and quantifying nitrate ions through the oxidation and reduction of Co^{2+}/Co^{3+} inside VB12. The C-GO-VB12 sensor was validated by detecting nitrate ions in the sap extracted from the cut stalk of maize plants and the method should easily transfer to many other plants with agricultural importance. Due to the high stability of C-GO-VB12, the sensor exhibited a year-long shelf lifetime at room temperature with no noticeable performance degradation. Further, the sensor was shaped into a needle using MEMS technology for *in situ* stalk nitrate measurement inside the plant, thus eliminating the need for time-consuming sample preparation procedures. The MEMS needle sensor broke plant tissues during insertion and detected nitrate concentrations at the ruptured region, including xylem and phloem tissues as well as other plant cells. It should be pointed out that nitrate transport is likely limited to the xylem as the xylem transports nutrients, including nitrate, and water from the roots to aboveground organs, whereas the phloem transports sugars.[41] Consistent with our results in Figure 8d, previous work focusing on xylem nitrate transport in maize showed that the concentration of nitrate in the xylem generally increases with the nitrogen fertilizer input to the soil.[42]

The laser writing-enabled selective pyrolysis, in conjunction with the photo patternable epoxy bioresin modified with two-dimensional (2D) materials and artificial enzymes, will shed

https://doi.org/10.1021/acsami.2c01988
ACS Appl. Mater. Interfaces XXXX, XXX, XXX−XXX

light on potentially monolithic integration of carbon-based electrochemical sensors and electronic circuits on a single chip. Because a high-temperature laser beam spot is applied only to the area of interest, other areas of the same substrate will be minimally affected, thus potentially making it a means of post-CMOS processing to realize carbon-based sensing electrodes on silicon wafers. In addition, manufacturing scalability will be achieved by incorporating the selective pyrolysis method with conventional spatial light modulation techniques, such as digital micromirror devices, to perform simultaneous pyrolysis in different areas of the substrate. Furthermore, from a material innovation perspective, different photo patternable epoxy materials, 2D materials (*e.g.*, hexagonal boron nitride, molybdenum disulfide, tungsten ditelluride, phosphorene, and Xenes)[43] and artificial enzymes (containing macrocycles, such as cyclophanes, cavitands, and calixarenes) can also be incorporated to conduct catalytic reactions inside the pyrolytic carbon electrode. Also, with the help of wireless communication devices, the present nitrate sensors can blend into the Internet of Things for wirelessly monitoring *in planta* nitrate concentrations in the field. Our sensors, in conjunction with other agricultural sensors,[44] will provide the information on soil acidity, moisture, temperature, and other stresses, as inputs to crop models and artificial intelligence algorithms to not only predict how genetics, management practices, and the environment interact together to influence crop growth and yield but also help decision-making for farmers to adopt sustainable agricultural practices, including optimum fertilization,[45] irrigation,[46] and pesticide applications.[47] Lastly, by determining and applying appropriate redox potentials of different target molecules, it is possible to use the C-GO-VB12 sensor for detecting various species (*e.g.*, ammonium, nitrite, and phosphate ions) for a wide range of applications, such as agricultural resource management, environmental monitoring, and biomedical diagnostics.

4. EXPERIMENTAL SECTION

4.1. Chemicals. GO nanosheets (one to five atomic layers; conductivity: 500−700 S/m; Brunauer−Emmett−Teller (BET) surface area: 650−750 m^2/g) were obtained from ACS Material (Pasadena, CA). VB12 powder (purity: >98%; molecular weight: 1355.37 g/mol; formula: $C_{63}H_{88}CoN_{14}O_{14}P$) was obtained from Sigma Aldrich (St. Louis, MO). An SU8 photoresist (model: SU-8 2050) was obtained from Kayaku Advanced Materials (Woburn, MA). Deionized (DI) water (resistivity: 18.2 MΩ·cm) was homemade using a DI water generator (Millipore, Billerica, MA). Ethyl alcohol (200 proof) was purchased from Fisher Scientific (Hampton, NH). Standard solutions of nitrate ions used for sensor characterization were prepared by dissolving appropriate amounts of KNO_3 powder (Sigma Aldrich, St. Louis, MO) in DI water. All chemicals utilized in this work were of analytical grade and used as obtained without any purification.

4.2. Preparation of SU8-GO-VB12. To synthesize SU8-GO-VB12, 20 mg of GO nanosheets and 250 mg of VB12 powder were mixed in 3 mL of a mixture of ethanol and DI water (ethanol-to-water volume ratio: 7:3) and then sonicated for 2 h until the mixture solution of GO and VB12 became homogeneous. Subsequently, 10 mL of an SU8 photoresist solution was added to the above-prepared GO-VB12 mixture and then sonicated for another 4 h until the new mixture became homogeneous and no lumps were present. The SU8-GO-VB12 solution had a lower viscosity at 9033 cP, compared to the pure SU8 photoresist at 12593 cP (Table S2).

4.3. Photopatterning of SU8-GO-VB12. The SU8-GO-VB12 solution could be spin-coated on a silicon wafer to form a thin film of SU8-GO-VB12. Table S3 shows the film thickness of SU8-GO-VB12 as a function of the spin speed. To obtain a 50 μm thick SU8-GO-VB12 film, the spin speed was set to be 1500 rpm, which was about one-half the speed required for the same thickness of the SU8 photoresist. The hotplate temperature and rest time used in the soft bake of SU8-GO- VB12 at different film thicknesses were similar to those of the pure SU8. Because VB12 and GO reduced the efficiency of SU8-GO-VB12 in absorbing ultraviolet (UV; 365 nm wavelength; 100 mW light intensity) light during photolithography, the UV exposure time increased to 3000 s for SU8-GO-VB12, compared with 2150 s required for SU8 (Table S4). Post-exposure bake for the 50 μm thick SU8-GO-VB12 film was performed on a hotplate at 95 °C for 2 min. Lastly, an SU8 developer (Kayaku Advanced Materials, Woburn, MA) was utilized to remove unexposed SU8-GO-VB12 with sonication.

4.4. Laser Pyrolysis. A computer-controlled 3.32 W power laser beam (Kehui K40 CO_2 laser engraver; maximum power: 40 W) was used in pyrolysis. The scanning speed of the laser was set at 10 mm/s because this speed resulted in a low resistivity of ∼100 Ω.cm for pyrolytic carbon[48] (Figure S11).

4.5. Nitrate Sensor Fabrication. To fabricate the nitrate sensor with SU8-GO-VB12, a silicon wafer grown with a 1 μm thick thermal oxide layer was cleaned with the RCA cleaning method. Then, a layer of SU8 (SU8-2150; thickness: 50 μm) was spin-coated and patterned into the shapes of the reference electrode (RE) and counter electrode (CE). Next, a layer of SU8-GO-VB12 (thickness: 50 μm) was coated and patterned into the shape of the working electrode (WE) of the sensor. Subsequently, both the SU8 and SU8-GO-VB12 patterns were pyrolyzed with a laser beam to form the pyrolytic C-based RE and CE and the C-GO-VB12-based WE for the nitrate sensor.

4.6. Needle-Shaped In Situ Nitrate Sensor Fabrication. First, a 10-nm-thick Ti layer and a 100-nm-thick Au layer were e-beam evaporated on the surface of a 600-nm-thick thermal oxide layer grown on a silicon wafer (Figure S9). Then, the Au electrodes were patterned *via* photolithography and etched with an Au etchant (GE-8148; Transene; Danvers, MA). Subsequently, a 700-nm-thick Ag electrode was formed *via* e-beam evaporation, photolithography, and wet etching (Silver etchant TFS; Transene; Danvers, MA). Next, the patterned Ag was treated with a 0.1 mM KCl solution for 2 min to form the Ag/AgCl-based RE. To form the C-GO-VB12 electrode, the SU8-GO-VB12 photoresist was spin-coated and then photopatterned, followed by the selective laser pyrolysis of SU8-GO-VB12 at the surface of the WE. Next, the needle was formed by deep reactive etching of silicon. Lastly, the needle sensor was wire-bonded to a printed circuit board for easy handling and connecting to external readout circuits.

■ ASSOCIATED CONTENT

Supporting Information

The Supporting Information is available free of charge at https://pubs.acs.org/doi/10.1021/acsami.2c01988.

Details of characterization, fabrication, measurement methods: characterization tools; determination of process parameters used in photolithography and laser pyrolysis of SU8-GO-VB12; cyclic voltammograms of the oxidation peak current *versus* scan rate; cyclic voltammograms of the C-GO-VB12 sensor responding to various nitrate concentrations; process flow for manufacturing of the MEMS needle sensor; and electrochemical impedance spectroscopy measurements of the MEMS needle sensor (PDF)

■ AUTHOR INFORMATION

Corresponding Author

Liang Dong − *Department of Electrical & Computer Engineering, Iowa State University, Ames, Iowa 50011, United States; Microelectronics Research Center, Iowa State*

https://doi.org/10.1021/acsami.2c01988
ACS Appl. Mater. Interfaces XXXX, XXX, XXX−XXX

University, Ames, Iowa 50011, United States; orcid.org/0000-0002-0967-4955; Email: ldong@iastate.edu

Authors

Hussam Ibrahim − *Department of Electrical & Computer Engineering, Iowa State University, Ames, Iowa 50011, United States; Microelectronics Research Center, Iowa State University, Ames, Iowa 50011, United States;* orcid.org/0000-0003-0458-3795

Shihao Yin − *Department of Electrical & Computer Engineering, Iowa State University, Ames, Iowa 50011, United States; Microelectronics Research Center, Iowa State University, Ames, Iowa 50011, United States;* orcid.org/0000-0003-0873-7114

Satyanarayana Moru − *Department of Electrical & Computer Engineering, Iowa State University, Ames, Iowa 50011, United States;* orcid.org/0000-0003-4301-0383

Yunjiao Zhu − *Agronomy Department, Iowa State University, Ames, Iowa 50011, United States;* orcid.org/0000-0001-9966-615X

Michael J. Castellano − *Agronomy Department, Iowa State University, Ames, Iowa 50011, United States;* orcid.org/0000-0003-1411-7931

Complete contact information is available at: https://pubs.acs.org/10.1021/acsami.2c01988

Author Contributions

L.D. conceived the sensor concept; H.I. and L.D. designed the experiments; H.I. and S.M. synthesized and characterized C-GO-VB12; S.Y. and H.I. studied the laser-induced graphene preparation and fabricated the sensors; H.I. conducted the electrochemical characterization for the sensor; H.I., Y.Z., and M.J.C. conducted the field experiments; and Y.Z. conducted spectrophotometry studies. All authors analyzed the data, discussed the result, and commented on the manuscript.

Notes

The authors declare no competing financial interest.

■ ACKNOWLEDGMENTS

The information, data, or work presented herein was funded in part by the Advanced Research Projects Agency-Energy (ARPA-E), U.S. Department of Energy, under award number DE-AR0000824; in part by the U.S. Department of Agriculture under grant numbers 2018-67021-27845, Grant 2020- 67021-31528, and Grant 2020-68013-30934; in part by the U.S. National Science Foundation under Grant CNS-2125484; and in part by the Plant Sciences Institute at Iowa State University. The authors claim no conflict of interest and share equal contributions. The authors thank Dr. Patrick S. Schnable for the discussion and Lisa Coffey for her assistance with plant care.

■ REFERENCES

(1) Blumenthal, J. M.; Baltensperger, D. D.; Cassman, K. G.; Mason, S. C.; Pavlista, A. D. Importance and Effect of Nitrogen on Crop Quality and Health. *Nitrogen Environ.* **2008**, 51−70.

(2) Bowles, T. M.; Atallah, S. S.; Campbell, E. E.; Gaudin, A. C. M.; Wieder, W. R.; Grandy, A. S. Addressing Agricultural Nitrogen Losses in a Changing Climate. *Nat. Sustainability* **2018**, *1*, 399−408.

(3) Snyder, C. S.; Bruulsema, T. W.; Jensen, T. L.; Fixen, P. E. Review of Greenhouse Gas Emissions from Crop Production Systems and Fertilizer Management Effects. *Agric., Ecosyst. Environ.* **2009**, *133*, 247−266.

(4) Castellano, M. J.; Archontoulis, S. V.; Helmers, M. J.; Poffenbarger, H. J.; Six, J. Sustainable Intensification of Agricultural Drainage. *Nat. Sustainability* **2019**, *2*, 914−921.

(5) Binford, G. D.; Blackmer, A. M.; El-Hout, N. M. Tissue Test for Excess Nitrogen during Corn Production. *Agron. J.* **1990**, *82*, 124−129.

(6) Padilla, F. M.; Gallardo, M.; Peña-Fleitas, M. T.; de Souza, R.; Thompson, R. B. Proximal Optical Sensors for Nitrogen Management of Vegetable Crops: A Review. *Sensors* **2018**, *18*, 2083.

(7) Fox, R. H.; Walthall, C. L. Crop Monitoring Technologies to Assess Nitrogen Status. *Agron. Monogr.* **2008**, 647−674.

(8) Balkcom, K. S.; Blackmer, A. M.; Hansen, D. J.; Morris, T. F.; Mallarino, A. P. Testing Soils and Cornstalks to Evaluate Nitrogen Management on the Watershed Scale. *J. Environ. Qual.* **2003**, *32*, 1015−1024.

(9) Continuous in situ Soil Nitrate Sensors: The Importance of High-Resolution Measurements Across Time and a Comparison with Salt Extraction-Based Methods - ProQuest. https://www.proquest.com/docview/2554444930?pq-origsite=gscholar&fromopenview=true (accessed April 27, 2022).

(10) Chen, Y.; Tang, Z.; Zhu, Y.; Castellano, M. J.; Dong, L. Miniature Multi-Ion Sensor Integrated with Artificial Neural Network. *IEEE Sens. J.* **2021**, *21*, 25606−25615.

(11) Minami, T.; Sasaki, Y.; Minamiki, T.; Wakida, S.; Kurita, R.; Niwa, O.; Tokito, S. Selective Nitrate Detection by an Enzymatic Sensor Based on an Extended-Gate Type Organic Field-Effect Transistor. *Biosens. Bioelectron.* **2016**, *81*, 87−91.

(12) Harnsoongnoen, S.; Wanthong, A.; Charoen-In, U.; Siritaratiwat, A. Microwave Sensor for Nitrate and Phosphate Concentration Sensing. *IEEE Sens. J.* **2019**, *19*, 2950−2955.

(13) Kodaira, M.; Shibusawa, S. Using a Mobile Real-Time Soil Visible-near Infrared Sensor for High Resolution Soil Property Mapping. *Geoderma* **2013**, *199*, 64−79.

(14) Xu, Z.; Wang, X.; Weber, R. J.; Kumar, R.; Dong, L. Nutrient Sensing Using Chip Scale Electrophoresis and in Situ Soil Solution Extraction. *IEEE Sens. J.* **2017**, *17*, 4330−4339.

(15) Ali, M. A.; Mondal, K.; Wang, Y.; Jiang, H.; Mahal, N. K.; Castellano, M. J.; Sharma, A.; Dong, L. In Situ Integration of Graphene Foam−Titanium Nitride Based Bio-Scaffolds and Microfluidic Structures for Soil Nutrient Sensors. *Lab Chip* **2017**, *17*, 274−285.

(16) Yang, H. Enzyme-Based Ultrasensitive Electrochemical Biosensors. *Curr. Opin. Chem. Biol.* **2012**, *16*, 422−428.

(17) Monteiro, T.; Almeida, M. G. Electrochemical Enzyme Biosensors Revisited: Old Solutions for New Problems. *Crit. Rev. Anal. Chem.* **2019**, *49*, 44−66.

(18) Kobayashi, M.; Shimizu, S. Cobalt Proteins. *Eur. J. Biochem.* **1999**, *261*, 1−9.

(19) Romanholo, P. V. V.; Razzino, C. A.; Raymundo-Pereira, P. A.; Prado, T. M.; Machado, S. A. S.; Sgobbi, L. F. Biomimetic Electrochemical Sensors: New Horizons and Challenges in Biosensing Applications. *Biosens. Bioelectron.* **2021**, *185*, No. 113242.

(20) McCreery, R. L. Advanced Carbon Electrode Materials for Molecular Electrochemistry. *Chem. Rev.* **2008**, *108*, 2646−2687.

(21) Wang, Z.; Dai, Z. Carbon Nanomaterial-Based Electrochemical Biosensors: An Overview. *Nanoscale* **2015**, *7*, 6420−6431.

(22) Singh, A.; Jayaram, J.; Madou, M.; Akbar, S. Pyrolysis of Negative Photoresists to Fabricate Carbon Structures for Microelectromechanical Systems and Electrochemical Applications. *J. Electrochem. Soc.* **2002**, *149*, No. E78.

(23) Xu, H.; Malladi, K.; Wang, C.; Kulinsky, L.; Song, M.; Madou, M. Carbon Post-Microarrays for Glucose Sensors. *Biosens. Bioelectron.* **2008**, *23*, 1637−1644.

(24) Mamidi, S.; Gangadharan, A.; Sharma, C. S. Fabrication of Three Dimensional Hierarchical Carbon Microelectrodes as High-Performance Anode for Lithium-Ion Batteries. *ECS Meet. Abstr.* **2020**, *MA2020-01*, 318.

(25) Amato, L.; Heiskanen, A.; Caviglia, C.; Shah, F.; Zór, K.; Skolimowski, M.; Madou, M.; Gammelgaard, L.; Hansen, R.; Seiz, E.

G.; Ramos, M.; Moreno, T. R.; Martínez-Serrano, A.; Keller, S. S.; Emnéus, J. Pyrolysed 3D-Carbon Scaffolds Induce Spontaneous Differentiation of Human Neural Stem Cells and Facilitate Real-Time Dopamine Detection. *Adv. Funct. Mater.* **2014**, *24*, 7042−7052.
(26) Martinez-Duarte, R.; Renaud, P.; Madou, M. J. A Novel Approach to Dielectrophoresis Using Carbon Electrodes. *Electrophoresis* **2011**, *32*, 2385−2392.
(27) Hassan, Y. M.; Caviglia, C.; Hemanth, S.; Mackenzie, D. M. A.; Alstrøm, T. S.; Petersen, D. H.; Keller, S. S. High Temperature SU-8 Pyrolysis for Fabrication of Carbon Electrodes. *J. Anal. Appl. Pyrolysis* **2017**, *125*, 91−99.
(28) Witvrouw, A. CMOS−MEMS Integration Today and Tomorrow. *Scr. Mater.* **2008**, *59*, 945−949.
(29) Ye, R.; James, D. K.; Tour, J. M. Laser-Induced Graphene: From Discovery to Translation. *Adv. Mater.* **2018**, *31*, No. 1803621.
(30) Ye, R.; Chyan, Y.; Zhang, J.; Li, Y.; Han, X.; Kittrell, C.; Tour, J. M. Laser-Induced Graphene Formation on Wood. *Adv. Mater.* **2017**, *29*, No. 1702211.
(31) Huang, L.; Su, J.; Song, Y.; Ye, R. Laser-Induced Graphene: En Route to Smart Sensing. *Nano-Micro Lett.* **2020**, *12*, No. 157.
(32) Ma, W.; Zhu, J.; Wang, Z.; Song, W.; Cao, G. Recent Advances in Preparation and Application of Laser-Induced Graphene in Energy Storage Devices. *Mater. Today Energy* **2020**, *18*, No. 100569.
(33) Zhang, G.; Han, Y.; Shao, C.; Chen, N.; Sun, G.; Jin, X.; Gao, J.; Ji, B.; Yang, H.; Qu, L. Processing and Manufacturing of Graphene-Based Microsupercapacitors. *Mater. Chem. Front.* **2018**, *2*, 1750−1764.
(34) Wang, M.; Yang, Y.; Gao, W. Laser-Engraved Graphene for Flexible and Wearable Electronics. *Trends Chem.* **2021**, *3*, 969−981.
(35) Zhang, J.; Zhang, F.; Yang, H.; Huang, X.; Liu, H.; Zhang, J.; Guo, S. Graphene Oxide as a Matrix for Enzyme Immobilization. *Langmuir* **2010**, *26*, 6083−6085.
(36) Ali, M. A.; Jiang, H.; Mahal, N. K.; Weber, R. J.; Kumar, R.; Castellano, M. J.; Dong, L. Microfluidic Impedimetric Sensor for Soil Nitrate Detection Using Graphene Oxide and Conductive Nanofibers Enabled Sensing Interface. *Sens. Actuators, B* **2017**, *239*, 1289−1299.
(37) Jo, W.-K.; Moru, S.; Tonda, S. Cobalt-Coordinated Sulfur-Doped Graphitic Carbon Nitride on Reduced Graphene Oxide: An Efficient Metal−(N,S)−C-Class Bifunctional Electrocatalyst for Overall Water Splitting in Alkaline Media. *ACS Sustainable Chem. Eng.* **2019**, *7*, 15373−15384.
(38) Jin, J.; Fu, X.; Liu, Q.; Zhang, J. A Highly Active and Stable Electrocatalyst for the Oxygen Reduction Reaction Based on a Graphene-Supported G-C3N4@Cobalt Oxide Core−Shell Hybrid in Alkaline Solution. *J. Mater. Chem. A* **2013**, *1*, 10538.
(39) Loock, H.-P.; Wentzell, P. D. Detection Limits of Chemical Sensors: Applications and Misapplications. *Sens. Actuators, B* **2012**, *173*, 157−163.
(40) Ali, M. A.; Hong, W.; Oren, S.; Wang, Q.; Wang, Y.; Jiang, H.; Dong, L. Tunable Bioelectrodes with Wrinkled-Ridged Graphene Oxide Surfaces for Electrochemical Nitrate Sensors. *RSC Adv.* **2016**, *6*, 67184−67195.
(41) White, P. J. Chapter 3 - Long-distance Transport in the Xylem and Phloem. https://www.sciencedirect.com/science/article/pii/B9780123849052000030 (accessed Jan 16, 2022).
(42) Liao, C.; Liu, R.; Zhang, F.; Li, C.; Li, X. Nitrogen Under- and Over-Supply Induces Distinct Protein Responses in Maize Xylem SapF. *J. Integr. Plant Biol.* **2012**, *54*, 374−387.
(43) Mas-Ballesté, R.; Gómez-Navarro, C.; Gómez-Herrero, J.; Zamora, F. 2D Materials: To Graphene and Beyond. *Nanoscale* **2011**, *3*, 20−30.
(44) Ali, M. A.; Dong, L.; Dhau, J.; Khosla, A.; Kaushik, A. Perspective—Electrochemical Sensors for Soil Quality Assessment. *J. Electrochem. Soc.* **2020**, *167*, No. 037550.
(45) Ali, M. A.; Wang, X.; Chen, Y.; Jiao, Y.; Mahal, N. K.; Moru, S.; Castellano, M. J.; Schnable, J. C.; Schnable, P. S.; Dong, L. Continuous Monitoring of Soil Nitrate Using a Miniature Sensor with Poly(3-Octyl-Thiophene) and Molybdenum Disulfide Nanocomposite. *ACS Appl. Mater. Interfaces* **2019**, *11*, 29195−29206.
(46) Chen, Y.; Tian, Y.; Wang, X.; Wei, L.; Dong, L. Miniaturized, Field-Deployable, Continuous Soil Water Potential Sensor. *IEEE Sens. J.* **2020**, *20*, 14109−14117.
(47) Nehra, M.; Dilbaghi, N.; Marrazza, G.; Kaushik, A.; Sonne, C.; Kim, K.-H.; Kumar, S. Emerging Nanobiotechnology in Agriculture for the Management of Pesticide Residues. *J. Hazard. Mater.* **2021**, *401*, No. 123369.
(48) Yin, S.; Ibrahim, H.; Schnable, P. S.; Castellano, M. J.; Dong, L. A Field-Deployable, Wearable Leaf Sensor for Continuous Monitoring of Vapor-Pressure Deficit. *Adv. Mater. Technol.* **2021**, *6*, No. 2001246.

https://doi.org/10.1021/acsami.2c01988
ACS Appl. Mater. Interfaces XXXX, XXX, XXX−XXX